ACS APPLIED MATERIALS & INTERFACES

Research Article

www.acsami.org

# In Situ Synthesis of Water-Soluble Magnetic Graphitic Carbon Nitride Photocatalyst and Its Synergistic Catalytic Performance

Shouwei Zhang,[†,‡] Jiaxing Li,[*,†] Meiyi Zeng,[‡] Guixia Zhao,[†] Jinzhang Xu,[‡] Wenping Hu,[§] and Xiangke Wang[*,†]

[†]Key Laboratory of Novel Thin Film Solar Cells, Institute of Plasma Physics, Chinese Academy of Sciences, P.O. Box 1126, 230031 Hefei, P. R. China

[‡]School of Materials Science and Engineering, Hefei University of Technology, Hefei 230031, China

[§]Beijing National Laboratory for Molecular Sciences, Key Laboratory of Organic Solids, Institute of Chemistry, Chinese Academy of Sciences, Beijing 100190, P. R. China

Supporting Information

**ABSTRACT:** Water-soluble magnetic-functionalized graphitic carbon nitride (g-$C_3N_4$) composites were synthesized successfully by in situ decorating spinel $ZnFe_2O_4$ nanoparticles on g-$C_3N_4$ sheets (CN-ZnFe) through a one-step solvothermal method. The magnetic properties of CN-ZnFe can be effectively controlled via tuning the coverage density and the size of $ZnFe_2O_4$ nanoparticles. The results indicate that the CN-ZnFe exhibits excellent photocatalytic efficiency for methyl orange (MO) and fast separation from aqueous solution by magnet. Interestingly, the catalytic performance of the CN-ZnFe is strongly dependent on the loading of $ZnFe_2O_4$. The optimum activity of 160CN-ZnFe photocatalyst is almost 6.4 and 5.6 times higher than those of individual g-$C_3N_4$ and $ZnFe_2O_4$ toward MO degradation, respectively. By carefully investigating the influence factors, a possible mechanism is proposed and it is believed that the synergistic effect of g-$C_3N_4$ and $ZnFe_2O_4$, the smaller particle size, and the high solubility in water contribute to the effective electron−hole pairs separation and excellent photocatalytic efficiency. This work could provide new insights that g-$C_3N_4$ sheets function as good support to develop highly efficient g-$C_3N_4$-based magnetic photocatalysts in environmental pollution cleanup.

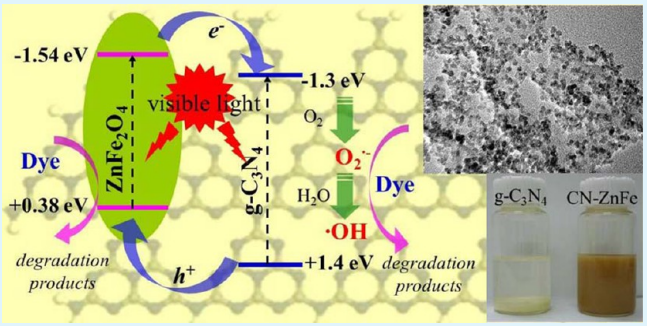


**KEYWORDS:** *g-$C_3N_4$/$ZnFe_2O_4$, highly water dispersible, tunable magnetic properties, charge separation, photocatalytic activity, degradation*

## 1. INTRODUCTION

Photocatalytic degradation of various organic pollutants by semiconductor as photocatalyst has attracted considerable interest in the past decades because it gives huge development potential for converting solar energy into chemical energy to decompose various harmful organic contaminants.[1] All environmentally friendly efficient photocatalysts always possess good separation of electron−hole pairs, fair response to visible light, and suitable band gap for maximally utilizing sunlight energy. Up to now, most studies have focused on $TiO_2$ for its resistance to photocorrosion, peculiarities of chemical inertness, nontoxicity, and low cost.[2] However, $TiO_2$ is a wide-band-gap semiconductor (3.2 eV for anatase) and just absorbs 3−5% of sunlight in the UV region, which limits its application greatly.[3] Therefore, it is very important to develop visible-light-driven photocatalysts to improve sunlight utilization.

Recently, the nontoxic and abundant g-$C_3N_4$ materials have attracted much attention and have frequently been used as metal-free photocatalysts for solar energy conversion, environment purification, and hydrogen production.[4−6] However, there are also many drawbacks for the g-$C_3N_4$ materials, which include (a) high photogenerated electron−hole recombination rate, (b) low specific surface area, and (c) the band gap (2.7 eV), negligible absorption above 460 nm in solar spectra. To solve these problems, it is favorable to combine g-$C_3N_4$ with other semiconductors with suitable band gap to extend the absorption range of g-$C_3N_4$. Meanwhile, heterojunctions that were formed between different semiconductor materials could provide great potential driving force to improve the separation of electon−hole pairs, such as BiOBr-carbon nitride,[7] $Bi_2WO_6$/g-$C_3N_4$,[8] and GO/g-$C_3N_4$,[9] which were proven to be effective photocatalysts to degrade various organic pollutants (such as MO and Rhodamine B) under visible light irradiation. And the novel AuNP/g-C3N4 and $Bi_2WO_6$/g-$C_3N_4$ composite photocatalysts were just prepared and used for the photodegradation of MO.[10,11] Niu et al. prepared g-$C_3N_4$ nanosheets through

Received: September 22, 2013
Accepted: November 19, 2013
Published: November 19, 2013

  

direct thermal oxidation of bulk g-$C_3N_4$ in air, which improved electron transport ability and increased lifetime of photoexcited charge carriers.[12] Xie's group reported preparation of ultrathin graphitic-phase $C_3N_4$ nanosheets through a liquid exfoliation from bulk materials in water for the first time. This ultrathin nanosheets exhibit enhanced photoabsorption and photoresponse, so not only the intrinsical photocurrent and photocatalytic activity but also the photoluminescence (PL) quantum yield were improved.[13] Graphitic carbon nitride nanosheets are extracted and produced by simple liquid-phase (use isopropanol) exfoliation of layered bulk materials, and exhibit good photocatalytic activity for the hydrogen evolution under visible light.[14]

However, the use of these photocatalysts for photocatalysis is often limited due to the easy loss of the suspended particulate catalysts in the process of photocatalytic reaction and separation. Ye et al.[15] first reported the simple fabrication of magnetically separable carbon nitride photocatalyst ($Fe_2O_3$/g-$C_3N_4$), for degradation of Rhodamine B. However, due to the poor control over the catalyst size, size distribution, and location of magnetic nanoparticles on the g-$C_3N_4$ sheets, the prepared $Fe_2O_3$/g-$C_3N_4$ composites may agglomerate and gradually precipitate from their aqueous suspension.

Spinel $ZnFe_2O_4$ with a relatively narrow band gap of 1.9 eV has attracted considerable attention in the fields of solar transformation, photocatalysis, and hydrogen evolution due to its visible-light response, high stability, easy synthesis, and low cost.[16,17] It was reported that the $ZnFe_2O_4$ functionalized BiOBr heterojunctions exhibited excellent photocatalytic activity in degradation of Rhodamine B under visible light irradiation.[18] A well-aligned $ZnFe_2O_4$/$TiO_2$ nanotube array electrode was also successfully prepared through a two-step electrochemical process of anodization and cathodic electrodeposition method. And this electrode showed greatly enhanced electrochemically assisted photocatalytic activity for the decomposition of chlorinated organic compounds under visible light irradiation.[19] Recently, $ZnFe_2O_4$ multiporous microbricks hybrid was synthesized via a facile deposition-precipitation reaction and showed much higher photocatalytic activity in degradation of 4-chlorophenol.[20] Clearly, as a magnetic semiconductor material, $ZnFe_2O_4$ might not only prevent the agglomeration of the catalyst nanoparticles during recovery, but also offer some synergetic enhancement of the catalytic activity by forming the hybrid structure.

Herein, we report for the first time a novel, inexpensive and simple one-step solvothermal route to synthesize superparamagnetic and water-soluble g-$C_3N_4$/$ZnFe_2O_4$ (CN-ZnFe) heterojunctions composites with controlled coverage density. The obtained CN-ZnFe composites show enhanced photocatalytic performance for the degraded MO in water under visible light irradiation, higher than those of pure g-$C_3N_4$ and $ZnFe_2O_4$ materials. Our study provides new insights that g-$C_3N_4$ sheets function as good support to develop high performance of g-$C_3N_4$-based magnetic photocatalysts and facilitate their practical applications in environmental issues.

## 2. EXPERIMENTAL SECTION

The synthesis, characterization of g-$C_3N_4$ and CN-ZnFe composites, and photocatalytic degradation experiments are all listed in the Supporting Information.

## 3. RESULTS AND DISCUSSION

In this work, we report an in situ growth strategy for the synthesis of a CN-ZnFe composite (as shown in Scheme 1).

**Scheme 1. Illustration of the Synthesis Process of g-$C_3N$/$ZnFe_2O_4$ Composites (for clarity, sizes are not represented proportionally)**

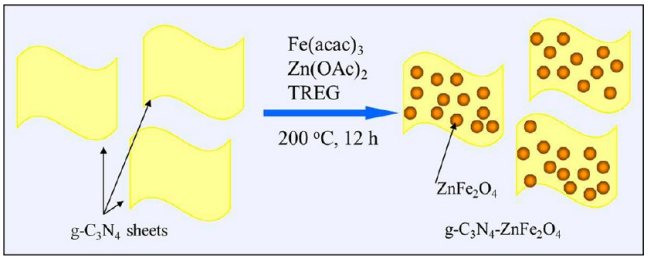


Metal salt [$Fe(acac)_3$ and $Zn(CH_3COO)_2{\cdot}2H_2O$] solutions were mixed with ultrasonically dispersed g-$C_3N_4$ sheets in triethylene glycol (TREG) solution. After solvothermal reaction, finely distributed uniform magnetic $ZnFe_2O_4$ nanoparticles were less than 10 nm in size and successfully deposited on the surface of g-$C_3N_4$ sheets. During the reaction, TREG acted as a stabilizer to prevent further gathering and agglomeration of the subparticles to give monodisperse spherical $ZnFe_2O_4$ nanoparticles.

The XRD patterns of the g-$C_3N_4$ and 160CN-ZnFe photocatalysts are shown in Figure 1A. In the case of g-$C_3N_4$, the strong peak located at 27.21° was the typical interplanar stacking peak of conjugated aromatic systems. The other peak at 12.81° belongs to an in-planar structural packing motif. Both peaks were the characteristic peaks commonly found in carbon nitride.[21] Compared to the pure g-$C_3N_4$, six new peaks at 30.1, 35.4, 42.7, 53.2, 56.7, and 62.3 were observed for 160CN-ZnFe, which match well with the (220), (311), (400), (422), (511), and (440) crystal planes of the standard XRD data for the bulk cubic spinel structure $ZnFe_2O_4$ (JCPDS file no. 22-1012) (Figure 1A).[22] No impurities are observed, which indicated that a g-$C_3N_4$/$ZnFe_2O_4$ composite was formed during the solvothermal process. The average size of the as-synthesized $ZnFe_2O_4$ nanoparticles on g-$C_3N_4$ sheets was calculated to be 5.8 nm from the width of the strongest diffraction line (311) by using the Debye−Scherrer formula.

UV−vis spectra of g-$C_3N_4$ and CN-ZnFe composites are shown in Figure 1B. The CN-ZnFe composites showed a broad and strong absorption in the visible light region. This result indicated that CN-ZnFe could absorb more photons and were beneficial to the photocatalytic process. In comparison to the pure g-$C_3N_4$, the band edge positions of CN-ZnFe composites exhibited a small red shift and the absorption intensity of the composites also became stronger with increasing $ZnFe_2O_4$ content. The UV−vis results indicated that more photogenerated charges were generated when CN-ZnFe composites were excited under visible light irradiation, which will enhance the photocatalytic performance.

The FTIR spectra of g-$C_3N_4$ and CN-ZnFe photocatalysts are shown in Figure 1C. In the FTIR spectrum of g-$C_3N_4$, the bands at 1640.5, 1569.1, 1462.1, and 1412.2 $cm^{-1}$ were assigned to typical stretching vibration modes of the heptazine-derived repeating units.[23] The intense band at 812.1 $cm^{-1}$ represented the out-of-plane bending vibration characteristic of heptazine rings. The bands at 1321.8 and 1243.3 $cm^{-1}$

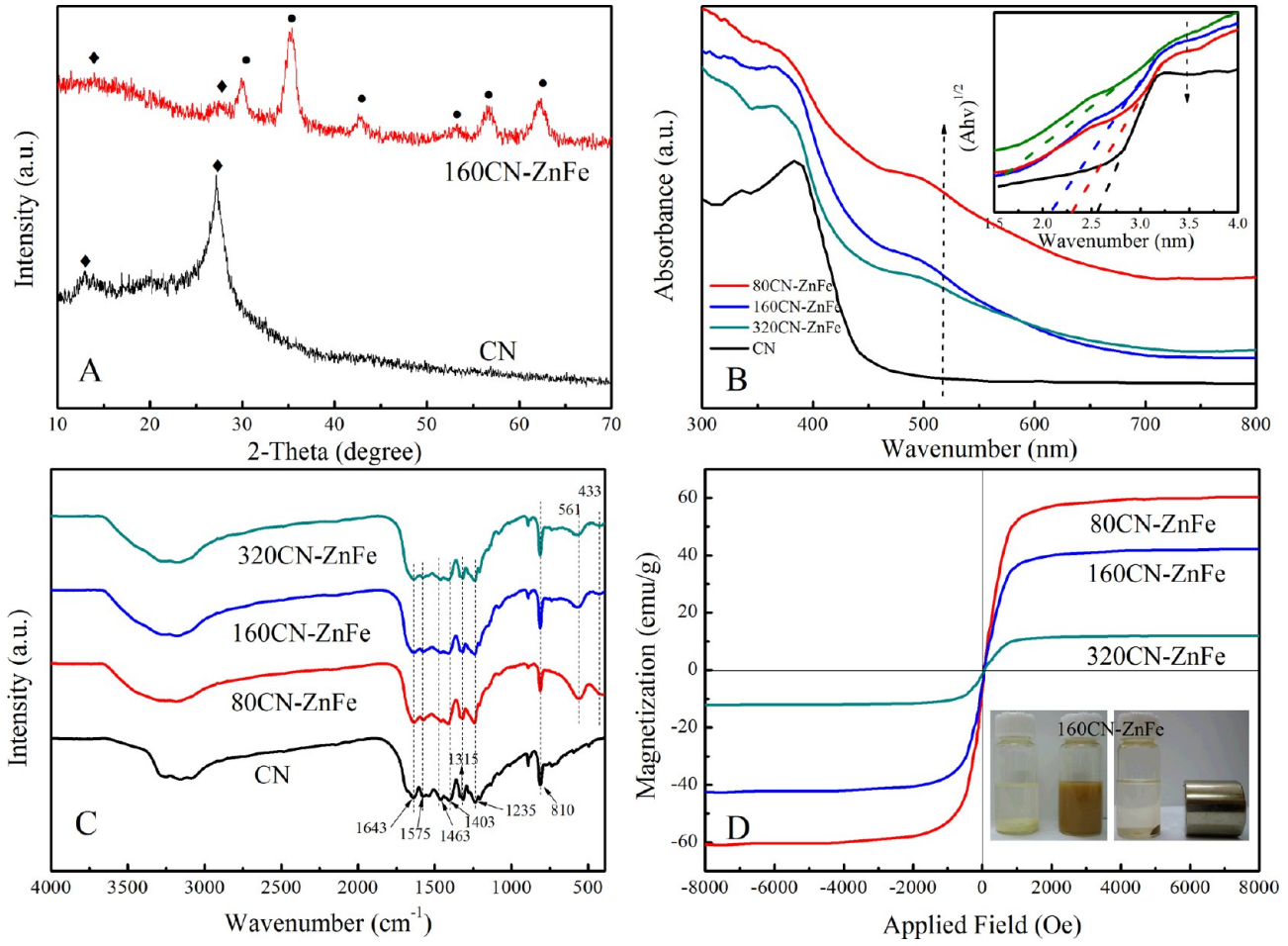


**Figure 1.** (A) XRD patterns, (B) UV–vis DRS, (C) FTIR, and (D) magnetization curves of the photocatalysts. Inset pictures show the composite with a stable, brown aqueous dispersion and easy separation by magnet.

corresponded to stretching vibration of connected units of C–N(–C)–C (full condensation) or C–NH–C (partial condensation), which was also supported by the stretching vibration modes of the broad weak band around 3235.9 $cm^{-1}$ for hydrogen-bonding interactions. The broad band at 3000–3700 $cm^{-1}$ belonged to the N–H vibration due to partial condensation and the adsorbed water molecules. Two bands at 446 and 563 $cm^{-1}$ corresponded to the vibration of metal ions at the octahedral and tetrahedral sites in $ZnFe_2O_4$, respectively.[24] All the characteristic peaks of g-$C_3N_4$ and $ZnFe_2O_4$ were observed in the CN-ZnFe composite photocatalyst.

The magnetic properties of CN-ZnFe were also studied. As shown in Figure 1D, the coercivity force was almost ignored at RT, which indicated that CN-ZnFe composite was magnetic. It can be calculated that the $M_s$'s were about 10.2, 40.6, and 63.8 emu/g for 320CN-ZnFe, 160CN-ZnFe, and 80CN-ZnFe, respectively, which concluded that the magnetic properties of CN-ZnFe could be well tuned by adjusting the decoration of $ZnFe_2O_4$ nanoparticles with high crystallinity on g-$C_3N_4$ sheets by changing reaction conditions. In addition, as observed from the inset image, the magnetic $ZnFe_2O_4$ could form a stable suspension in aqueous solution, and also it could be separated easily by magnets. This result clearly indicated that this kind of magnetic g-$C_3N_4$-based composite should be an excellent recyclable photocatalyst for environmental applications. The Brunauer–Emmett–Teller (BET) surface area of CN-ZnFe (49.8 m2/g) was higher than that of CN (25.6 $m^2/g$) (Figure S1, Supporting Information).

The compositions of the g-$C_3N_4$ and CN-ZnFe were investigated by XPS, which showed the g-$C_3N_4$ was mainly composed of C and N elements (Figure 2A). The negligible amount of oxygen element could be ascribed to the tiny amount of $O_2$ adsorbed on the surface of the synthetic product during the polymerization process, which was a common phenomenon in the synthetic g-$C_3N_4$ materials. As shown in Figure 2B, the peaks of 1044.4 and 1022.8 eV were ascribed to Zn $2p_{1/2}$ and Zn $2p_{3/2}$, respectively. Furthermore, two peaks of Fe 2p located at 710.6 and 724.4 eV should be attributed to the spectra of Fe $2p_{3/2}$ and Fe $2p_{1/2}$ (Figure 2C). In Figure 2D, the N 1s spectrum could be fitted into four binding energies. Two main signals at 398.5 and 399.3 eV were exhibited. The former peak showed occurrence of C–N=C groups (denoted as $N_1$).[22] The second peak is related to either N–$(C)_3$ groups linking structural motif ($C_6N_7$) or amino groups ($(C)_2$–N–H) connecting with structural defects and incomplete condensation (denoted as $N_2$). The 401.0 eV peak was weak and corresponded to N of N–$(C)_3$ in the aromatic cycles. The 404.3 eV peak was attributed to the $\pi$-excitations.[25]

From the scanning electron microscopy (SEM) image of g-$C_3N_4$ (Figure 3A), those sheets were well dispersed on the substrate, ranging from hundreds of nanometers to several micrometers. Its surface was quite rough and uniformly covered by magnetic $ZnFe_2O_4$ naoparticles (Figure 3B). The trans-

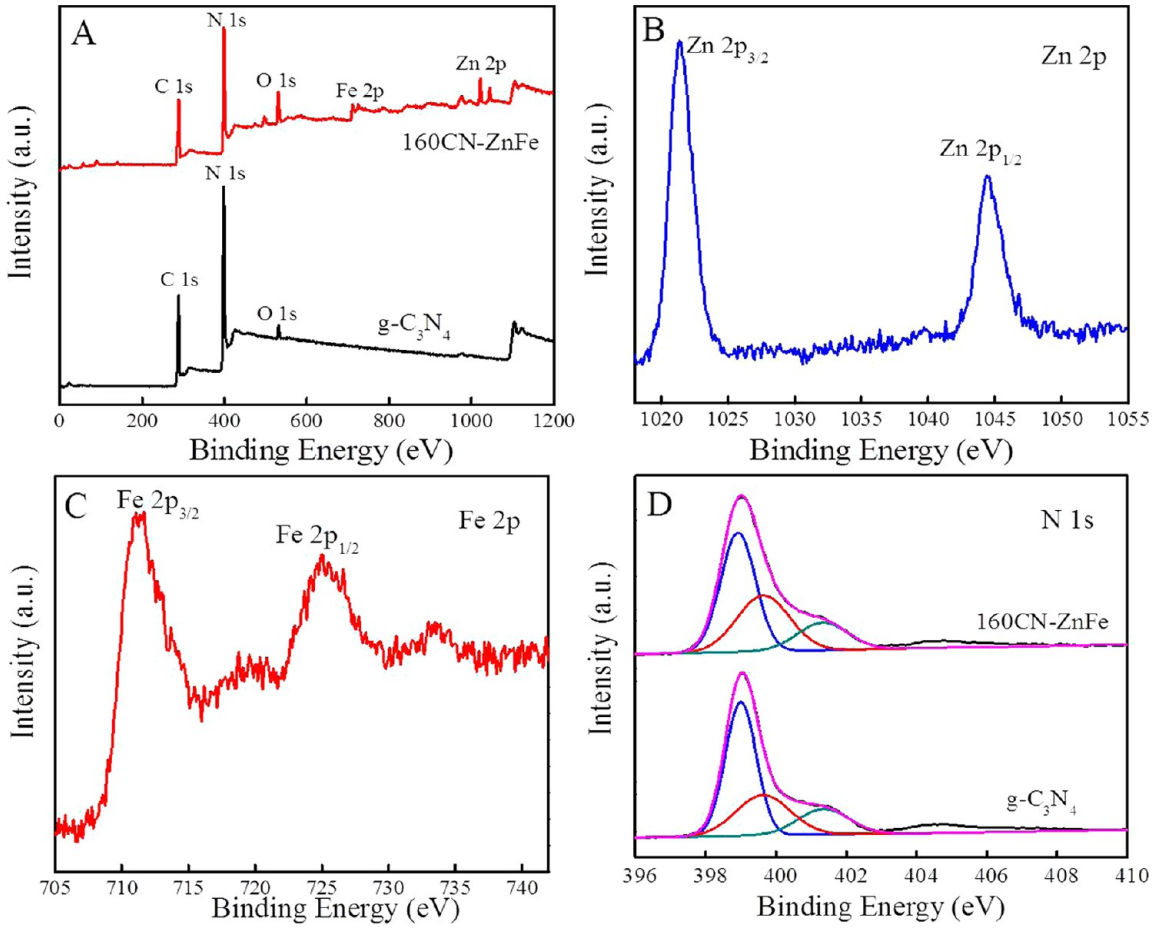


**Figure 2.** XPS spectra of the photocatalyst: (A) whole XPS spectra of g-$C_3N_4$ and 160CN-ZnFe composite, (B) Zn 2p and (C) Fe 2p of 160CN-ZnFe composite, and (D) N 1s of g-$C_3N_4$ and 160CN-ZnFe composite.

mission electron microscopy (TEM) image of g-$C_3N_4$ is shown in Figure 3C, where a two-dimensional sheetlike structure consisting of wrinkles could be observed in the g-$C_3N_4$, which was the analogue of crumpled graphene. Figure 3D revealed the detailed distribution of the magnetic $ZnFe_2O_4$ nanoparticles on g-$C_3N_4$ sheets. It can be seen that all the magnetic $ZnFe_2O_4$ nanoparticles were decorated on the surface of g-$C_3N_4$ sheets and the average size was ~5−6 nm. The magnetic $ZnFe_2O_4$ nanoparticles were distributed separately on g-$C_3N_4$ sheets as nanoislands, which could not only improve the dispersion property of layered materials but also offer more photocatalytic reaction sites, and heterojunction structure was formed. Therefore, the photocatalytic activity of CN-ZnFe was improved greatly. The interaction between $ZnFe_2O_4$ and g-$C_3N_4$ sheets was so strong that these nanoparticles could not peel off from the g-$C_3N_4$ sheets even under ultrasonication during the procedure of preparation TEM samples. Despite many $ZnFe_2O_4$ nanoparticles covered on the surface of g-$C_3N_4$, the sheets of g-$C_3N$ remained flat. From the high resolution TEM (HRTEM) image of CN-ZnFe (Figure 3E), the lattice fringe spacing was 0.487 nm, which was corresponded to the (111) lattice plane of a cubic $ZnFe_2O_4$. In addition, the EDS spectrum of CN-ZnFe shown in Figure 3F revealed the existence of Fe, Zn, C, O, and N elements in the composites, while the signal of Cu is from the copper grids.

As shown in Figure 4, the decoration of magnetic $ZnFe_2O_4$ nanoparticles on g-$C_3N_4$ sheets was obviously influenced by the initial weight ratios of $Fe(acac)_3$ to g-$C_3N_4$ sheets, When the ratio decreased to 1:1 (320CN-ZnFe), a large area was bare, and $ZnFe_2O_4$ nanoparticles with average sizes of ~3−4 nm can be seen in Figure 4B, compared with the sample of 160CN-ZnFe (the ratio is 2:1) (Figure 4C). However, the distribution of magnetic $ZnFe_2O_4$ nanoparticles was still uniform and monodisperse. When the ratio was increased to 4:1 (80CN-ZnFe), the coverage density of $ZnFe_2O_4$ nanoparticles on g-$C_3N_4$ sheets was further tuned and the average sizes of $ZnFe_2O_4$ nanoparticles increased to ~7−8 nm (Figure 4D). Most of the $ZnFe_2O_4$ nanoparticles were homogeneous distribution on the surface of g-$C_3N_4$ sheets, but few magnetic $ZnFe_2O_4$ nanoparticles were aggregated slightly for the high coverage density. As discussed above, it can be concluded that not only the uniform magnetic $ZnFe_2O_4$ nanoparticles were effectively decorated on g-$C_3N_4$ sheets through the simple solvothermal process, but also the loading degree and size of $ZnFe_2O_4$ particles could be controlled successfully by adjusting concentrations of g-$C_3N_4$ sheets or iron precursor.

Figure 5 shows the photocatalytic activity of CN-ZnFe composites with different content of magnetic $ZnFe_2O_4$ nanoparticles under visible light irradiation. From the blank test (Figure 5A), the concentration of MO remained the same within 180 min, confirming that MO was very stable and its photolysis could be ignored under visible light irradiation without catalysts. Pure g-$C_3N_4$ showed low photocatalytic activity, in which 36% of MO was decomposed after irradiation for 180 min. Similarly, only 44% of MO was degraded by $ZnFe_2O_4$ for the same irradiation time. Surprisingly, the

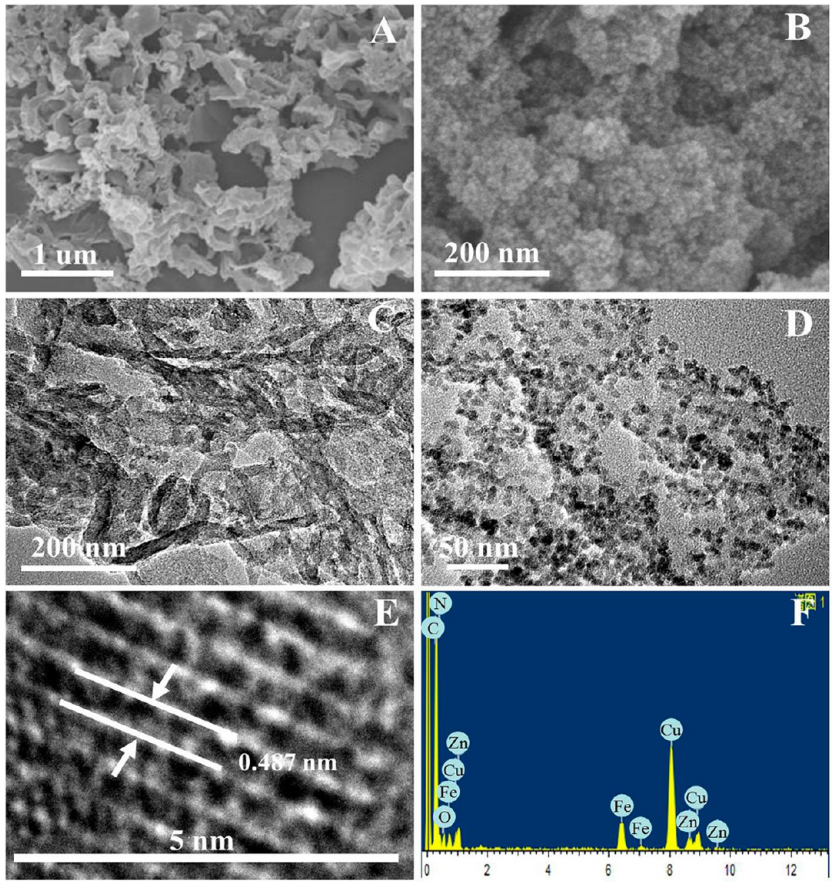


**Figure 3.** Characterization of g-$C_3N_4$ and 160CN-ZnFe composite: (A) g-$C_3N_4$ and (B) 160CN-ZnFe composite of SEM images, (C) g-$C_3N_4$ and (D) 160CN-ZnFe composite of TEM images, (E) HRTEM image of the $ZnFe_2O_4$ nanoparticle of the 160CN-ZnFe composite, and (F) EDS of the 160CN-ZnFe composite.

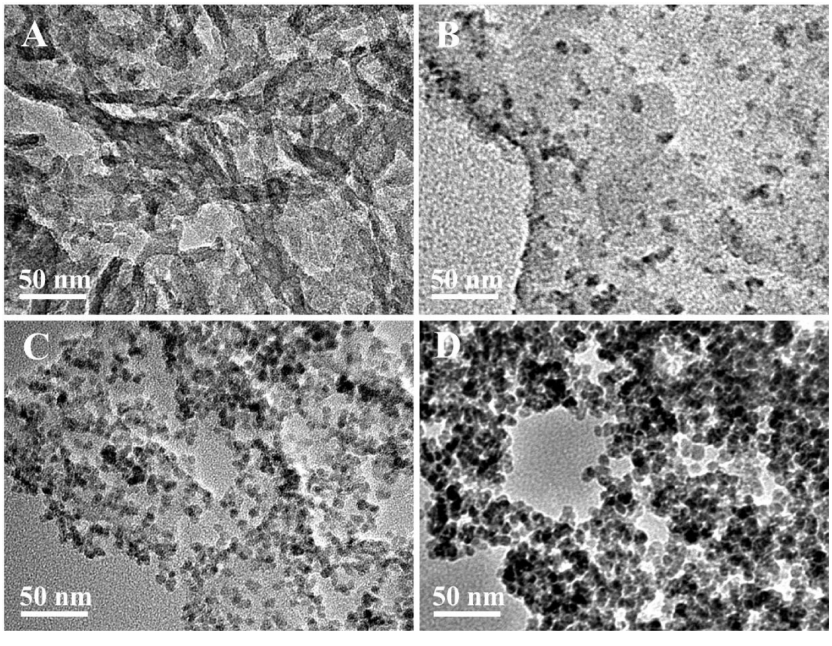


**Figure 4.** TEM images of synthesized CN-ZnFe composites with different initial weight g-$C_3N_4$ sheets, with the weight of reduced GO sheets unchanged. (A) Pure g-$C_3N_4$ sheets, (B) 320CN-ZnFe, (C) 160CN-ZnFe, and (D) 80CN-ZnFe, showing different coverage densities and particle sizes.

photocatalytic activity of CN-ZnFe composite reached ~98%. The results indicated that CN-ZnFe composite showed much higher photocatalytic activities than $ZnFe_2O_4$ and pure g-$C_3N_4$. Moreover, the photocatalytic activity of 160CN-ZnFe photo-

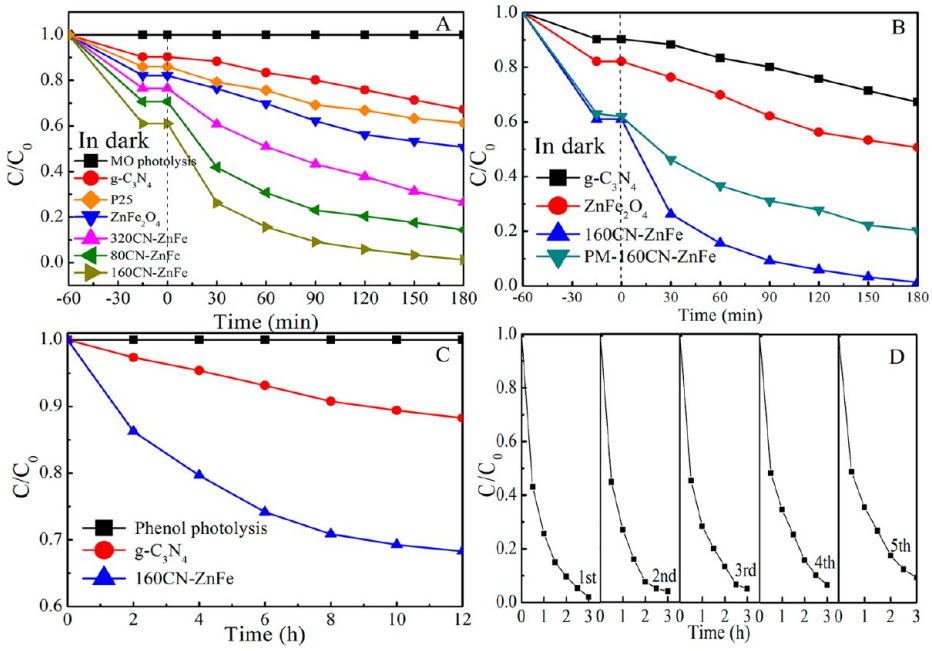


**Figure 5.** (A) Photocatalytic degradation of MO in aqueous solution over g-$C_3N_4$, P25, $ZnFe_2O_4$, and CN-ZnFe composites photocatalysts, (B) degradation of MO under visible light irradiation over different photocatalyst, (C) photocatalytic degradation of phenol over 160CN-ZnFe composite, pure g-$C_3N_4$ under visible light irradiation, and (D) recyclability of the 160CN-ZnFe photocatalyst in five successive experiments for the photocatalytic degradation of MO under visible light irradiation (no change in overall catalyst concentration for each cycle).

catalyst was 6.4 times higher than that of pure g-$C_3N_4$ and 5.6 times higher than that of pure $ZnFe_2O_4$. However, when the content of $ZnFe_2O_4$ was too high (such as 80CN-ZnFe), the photocatalytic activity decreased slightly, but it was still much higher than that of pure g-$C_3N_4$ and $ZnFe_2O_4$. The reason why excessive $ZnFe_2O_4$ decreased the photadegradation efficiency of CN-ZnFe composite could be concluded as follows: the high content of $ZnFe_2O_4$ could significantly affect the size and dispersion of $ZnFe_2O_4$ nanopaticles, which affect the photocatalytic activity. Previous research also indicated the dispersion and size of nanoparticles dotted on semiconductors surface could influence their photodegradation efficiency.[26−28] The smaller size and higher dispersibility of $ZnFe_2O_4$ on the g-$C_3N_4$ sheets meant higher photocatalytic activity. However, there would be negative effect when the coverage density was increased. The decrease of photodegradation efficiency of composites with higher $ZnFe_2O_4$ loading was closely related to the larger size of $ZnFe_2O_4$ nanoparticles. Larger nanoparticles could weaken the adhesion between $ZnFe_2O_4$ and g-$C_3N_4$ sheets, and thus the heterojunction structure would be damaged,[29] so when the coverage density of $ZnFe_2O_4$ was too high, the separation efficiency of photogenerated charges was low, leading to a decrease of photodegradation efficiency of CN-ZnFe. Therefore, only $ZnFe_2O_4$ nanoparticles coated on g-$C_3N_4$ with right size and dispersion can enhance the photocatalytic activity of g-$C_3N_4$ composites.

For further illustration of the effect and importance of interface between the components of CN-ZnFe heterojunction composites, the photocatalytic activities of 160CN-ZnFe and PM-160CN-ZnFe (the physical mixing of g-$C_3N_4$ and $ZnFe_2O_4$) were compared. Figure 5B shows that photodegardation efficiency of 160CN-ZnFe was always much higher than that of PM-160CN-ZnFe, which indicated definitely that the interface between g-$C_3N_4$ and $ZnFe_2O_4$ was very important to the photocatalytic activity. When PM-160CN-ZnFe was suspended in MO solution and stirred continuously, the isolated nanoparticles of g-$C_3N_4$ and $ZnFe_2O_4$ would collide with each other easily to induce the transient interfacial, as a result of relatively high possibility of photogenerated electrons transfer and electron−hole pair separation, rendering PM-160CN-ZnFe possess superior photocatalytic activity to g-$C_3N_4$ and $ZnFe_2O_4$. Different from the transient interfacial derived from those random collisions between the isolated nanoparticles of g-$C_3N_4$ and $ZnFe_2O_4$ in PM-160CN-ZnFe, the tight heterojunction structure of 160CN-ZnFe can stable facilitate interfacial electrons transfer and decrease the agglomeration and separation of g-$C_3N_4$ and $ZnFe_2O_4$. Moreover, as a representative colorless model organic pollutant, phenol was used to further evaluate the photodegradation efficiency of 160CN-ZnFe photocatalyst, as shown in Figure 5C. no obvious degradation of phenol was observed under direct visible light photolysis, and only 10% of phenol was degraded over bulk g-$C_3N_4$ under direct irradiation, while it is over 33% for 160CN-ZnFe, indicating that the CN-ZnFe was a kind of visible-light-driven photocatalyst with high efficiency. The pH effect of photocatalysis was also conducted (Figure S2).

The stability of a photocatalyst was also very important from the point of view of its practical application. The sample of 160CN-ZnFe was recycled for five times under the same reaction conditions. The sample was separated by using a magnet after each cycle, washed with 0.1 M $HNO_3$ and deionized water for several times, and then dried at 80 °C under vacuum. From Figure 5D, the photodegradation efficiency of 160CN-ZnFe decreased slightly in the five reuse cycles, which indicated that photocatalysts based on CN-ZnFe composites could be reused completely for wastewater treatment. We can see that the morphology of photocatalyst was slight agglomeration after reaction, but the structure and the dispersibility of the particles remains substantially after photocatalytic reaction (Figure S3). Therefore, we speculate

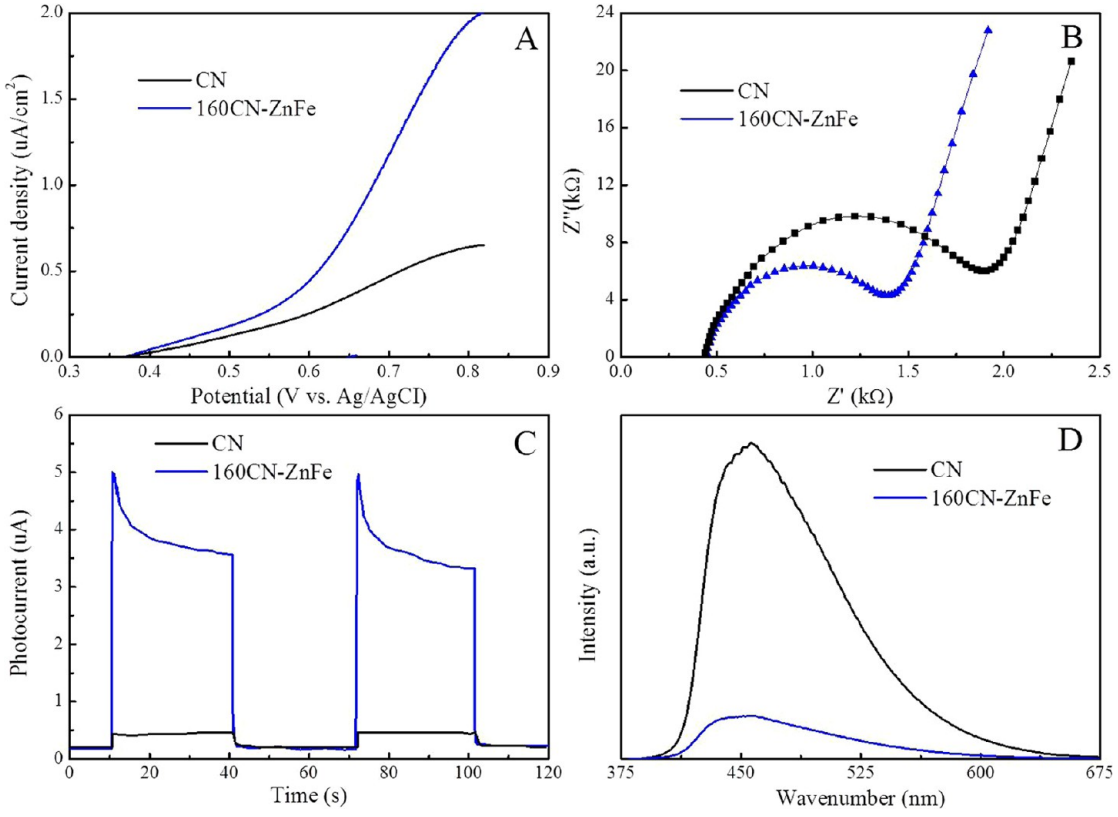


**Figure 6.** (A) Variation of photocurrent density vs bias potential (vs Ag/AgCl) of g-$C_3N_4$ and 160CN-ZnFe electrodes, (B) EIS changes of g-$C_3N_4$ and 160CN-ZnFe electrodes, (C) transient photocurrent responses of the g-$C_3N_4$, 160CN-ZnFe electrodes in 1 M $Na_2SO_4$ aqueous solution under visible light irradiation, and (D) PL spectra of g-$C_3N_4$, 160CN-ZnFe composite.

that the structure is stable in stirring condition and ultrasonic wave irradiation under our experiment condition. Therefore, CN-ZnFe composites can be used as one of reusable and stable visible-light photocatalysts with high-performance in the environmental protection.

A series of experiments were conducted to further understand the photogenerated electron−hole pairs separation and the electrons transfer performance between g-$C_3N_4$ and $ZnFe_2O_4$. Photocurrent density was measured to evaluate the charge separation capability of heterojunction composites under visible light irradiation. To avoid the effect of dark currents, we studied charge separation capability with a pure photocurrent, which can be calculated by subtracting the dark current from the total current.[30,31] Figure 6A shows the photocurrent density of 160CN-ZnFe increased with the applied potential in the range of 0.4−0.8 V, and the photocurrent density was apparently higher than the maximal photocurrent density of g-$C_3N_4$. That is, photogenerated electron−hole pairs were efficiently separated in space, resulting in reduced photogenerated charge recombination, corresponding to its enhanced photocurrent density. As shown in Figure 6B, the electrochemical impedance spectra (EIS) are presented as Nyquist plots, and it was observed that the diameter of the semicircle in the plot becomes shorter with the introduction of $ZnFe_2O_4$, which indicated a decrease in the charge-transfer resistance on the electrode surface leading to an effective electron−hole pair separation; as a result, 160CN-ZnFe showed higher photodegradation efficiency.[32−34] The transient photocurrent responses of g-$C_3N_4$ and 160CN-ZnFe electrodes were recorded (Figure 6C), and g-$C_3N_4$ showed almost no photocurrent response. On the contrary, the 160CN-ZnFe composite showed an obvious relatively stable current under visible light irradiation, which indicated that the recombination of electrons and holes was inhibited greatly and the separation of photogenerated charges at the interface between g-$C_3N_4$ and $ZnFe_2O_4$ was more effectively realized.[34] Figure 6D shows the PL spectra of the 160CN-ZnFe composite and pure g-$C_3N_4$ excited by 365 nm. The main emission peak of pure g-$C_3N_4$ was centered at about 456 nm, which was consistent with the reported result.[14] However, in the PL spectrum of 160CN-ZnFe composites, a weaker emission peak in the same position was detected, which indicated that the photogenerated charges recombination rate in 160CN-ZnFe composites was much lower than that in pure g-$C_3N_4$. That is, the recombination of photogenerated electron−hole pairs was greatly inhibited by the introduction of $ZnFe_2O_4$, which showed photogenerated electron−hole pair separation efficiency of the 160CN-ZnFe composite was indeed higher than that in pure g-$C_3N_4$.

As we known, effective electron−hole pair separation at the heterojunction interfaces can significantly improve photocatalytic performance of composite photocatalysts. Based on the CB/VB edge potentials, the band gap positions of g-$C_3N_4$ were determined at −1.3 and +1.4 eV, while the CB and VB of $ZnFe_2O_4$ were at −1.54 and +0.38 eV, respectively.[35−38] Therefore, under the visible light, both g-$C_3N_4$ and $ZnFe_2O_4$ in the CN-ZnFe composite absorbed more light and thus generated more charges. The description of this process could be as follows: photogenerated holes would be formed when electrons were excited from VB to CB of both $ZnFe_2O_4$ and g-$C_3N_4$. The photogenerated electrons in $ZnFe_2O_4$ could easily migrate to the g-$C_3N_4$ surface, and at the same time the holes generated in the VB of g-$C_3N_4$ could migrate to $ZnFe_2O_4$.

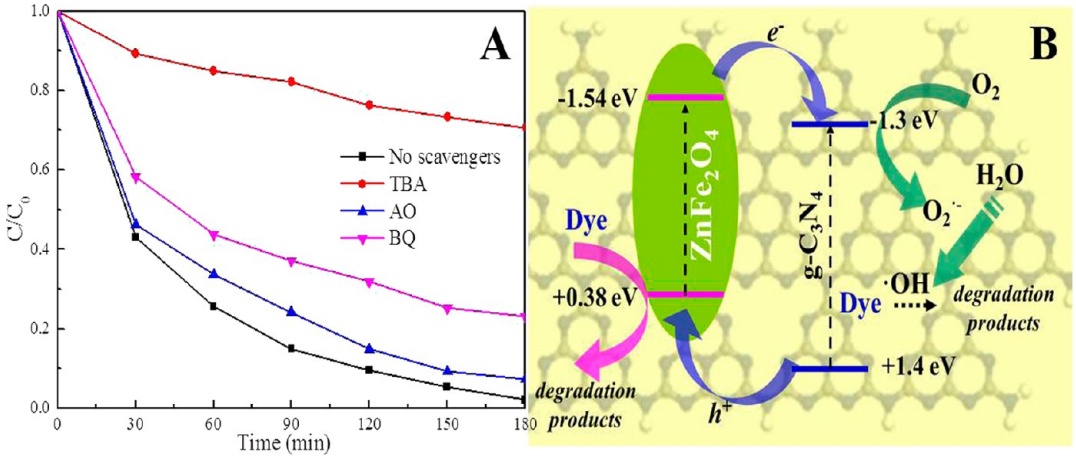


**Figure 7.** (A) Effects of different scavengers on the degradation of MO in the presence of 160CN-ZnFecomposite, and (B) band structure schematic of 160CN-ZnFe composite and possibly occurring reaction mechanism of MO on the surface of composite.

This process could improve effectively the photogenerated electron−hole pair separation and decrease greatly the possibility of photogenerated charge recombination. Therefore, $ZnFe_2O_4$ nanoparticles and g-$C_3N_4$ in the CN-ZnFe composite could form heterojunction structures, which lead to the improvement of photodegradation efficiency. As we know, the main active radicals are the photogenrated holes, ·OH radicals, and $\cdot O_2^-$ in the photocatalytic process. The transformation from $O_2$ to $\cdot O_2^-$ could be reduced by the electrons in CB on the surface of photocatalysts. The $\cdot O_2^-$ could react with holes generated reaction intermediates $H_2O_2$ under irradiation, and then to produce active ·OH radicals or be probable to form organic peroxides when organic scavengers were added into this system.[39] Therefore, to examine the role of these reactive species, a series of radicals trapping experiments were performed by using ammonium oxalate (AO), benzoquinone (BQ), and *tert*-butanol (TBA) scavengers as effective scavengers for holes, $\cdot O_2^-$, and ·OH radicals, respectively.[40,41] We observe to some extent that all of those scavengers result in the suppression of the degradation rate of MO, which indicates that holes, $\cdot O_2^-$, and ·OH radicals are indeed photogenerated on the surface of composites and function as oxidation sources. The possible photoreaction equations are as follows:

$$\text{CN} - \text{ZnFe} \xrightarrow{h\nu} \text{CN}\,(e^- \cdots h^+) - \text{ZnFe}\,(e^- \cdots h^+) \quad (1)$$

$$\text{CN}\,(e^- \cdots h^+) - \text{ZnFe}\,(e^- \cdots h^+) \xrightarrow{h\nu} \text{CN}\cdot e^- - \text{ZnFe}\cdot h^+ \quad (2)$$

$$e^- + O_2 \rightarrow \cdot O_2^- \quad (3)$$

$$\cdot O_2^- \rightarrow H_2O \rightarrow \cdot OH \quad (4)$$

$$e^- + H^+ + O_2 \rightarrow H_2O_2 \quad (5)$$

$$H_2O_2 + \cdot O_2^- \rightarrow \cdot OH + OH^- + O_2 \quad (6)$$

$$\cdot OH + \text{dye} \rightarrow \text{degradation products} \quad (7)$$

$$h^+ + \text{dye} \rightarrow \text{degradation products} \quad (8)$$

As the photogenerated electron−hole pairs separate in the composite photocatalyst, the photogenerated electrons transfer to the conduction band (CB) of the g-$C_3N_4$, and the holes in g-$C_3N_4$ migrate to the valence band (VB) of $ZnFe_2O_4$. For electrons, the CB potential of g-$C_3N_4$ (−1.3 eV vs NHE) is more negative than $E_0$ ($O_2/\cdot O_2^-$ = −0.13 eV vs NHE), which can produce $\cdot O_2^-$ radicals from dissolved $O_2$ by photogenerated electrons in g-$C_3N_4$. That is, the ·OH can be produced from electrons in CB potential of g-$C_3N_4$ via oxidation process.[42,43] However, for photogenerated holes, the VB potential of $ZnFe_2O_4$ (0.38 eV vs NHE) is more negative than ·OH/$OH^-$ (+1.99 eV). Therefore, no ·OH and $\cdot O_2^-$ production from the holes or electrons, and the major approach for degraded MO is oxidation of ·OH radicals based on the energy band theory analysis. In radical trapping experiments (Figure 7A), The degradation efficiency of MO decreased from 98% to 90% in the presence of AO compared to that with no radical scavengers, which indicated the photogenerated holes are not main sources for degradation of MO, nor the sources of ·OH radicals. In general, the more positive the valence band potential, the stronger the oxidation ability of photogenerated holes, which is favored for better photocatalytic activity.[42−44] So it can be concluded that direct oxidation by holes is negligible because the potential of photogenerated holes is not so positive that it cannot effectively oxidize dyes directly. Meanwhile, the degradation efficiencies of MO reach 27% and 75% in the presence of TBA and BQ, respectively, which indicates that ·OH radicals play a more crucial part than $\cdot O_2^-$ due to transformation of the majority of $\cdot O_2^-$ into ·OH radicals. Based on the above results, the reasonable photodegradation mechanism is shown in Figure 7B.

## 4. CONCLUSION

In conclusion, a facile synthetic strategy was developed for preparing magnetic $ZnFe_2O_4$ nanoparticle functionalized g-$C_3N_4$ sheets through a one-step solvothermal method. The coverage density and the size of $ZnFe_2O_4$ nanoparticles on g-$C_3N_4$ surface can control effectively the magnetic properties of CN-ZnFe composites. CN-ZnFe composites exhibit superior visible light photocatalysis, ascribing to the effective electron−hole pair separation at the composite interfaces, to the smaller particle size, to being highly water dispersible. This work could provide new insights that g-$C_3N_4$ sheets function as good support to develop highly efficient g-$C_3N_4$-based magnetic photocatalysts in environmental pollution cleanup.

## ■ ASSOCIATED CONTENT

### Supporting Information

Synthesis and characterization of g-$C_3N_4$ and CN-ZnFe composites; photocatalysis experiment; Figure S1 for $N_2$

adsorption−desorption isotherms of CN and 160CN-ZnFe; Figure S2 for pH effect of photocatalysis; Figure S3 for TEM image of the photocatalyst after photocatalytic reaction. This material is available free of charge via the Internet at http://pubs.acs.org.

## AUTHOR INFORMATION


### Corresponding Authors

*E-mail: lijx@ipp.ac.cn (J.L.). Fax: +86-551-65591310. Tel: +86-551-65592788.

*E-mail: xkwang@ipp.ac.cn (X.W.).


### Notes

The authors declare no competing financial interest.

## ACKNOWLEDGMENTS

The authors acknowledge the financial support from National Natural Science Foundation of China (21207136, 21225730, and 21272236) and the Ministry of Science and Technology of China (2011CB933700 and 2008CB417212).

## REFERENCES


(1) Ye, L. Q.; Liu, J. Y.; Jiang, Z.; Peng, T. Y.; Zan, L. *Appl. Catal., B* **2013**, *142*, 1−7.

(2) Chen, Y.; Regulacio, M. D.; Lim, S. H.; Xu, Q. H.; Han, M. Y. *Chem.—Eur. J.* **2012**, *18*, 11258−11263.

(3) Jiang, B. J.; Tian, C. G.; Zhou, W.; Wang, J. Q.; Xie, Y.; Pan, Q. J.; Ren, Z. Y.; Dong, Y. Z.; Fu, D.; Han, J. L.; Fu, H. G. *Chem.—Eur. J.* **2011**, *17*, 8379−8387.

(4) Hou, Y. D.; Laursen, A. B.; Zhang, J. S.; Zhang, G. D.; Zhu, Y. S.; Wang, X. C.; Dahl, S.; Chorkendorff, I. *Angew. Chem., Int. Ed.* **2013**, *52*, 3621−3625.

(5) Chen, L. C.; Huang, D. J.; Ren, S. Y.; Dong, T. Q.; Chi, Y. W.; Chen, G. N. *Nanoscale* **2013**, *5*, 225−230.

(6) Wang, Y.; Wang, X. C.; Antonietti, M. *Angew. Chem., Int. Ed.* **2012**, *51*, 68−69.

(7) Fu, J.; Tian, Y. L.; Chang, B. B.; Xi, F. N.; Dong, X. P. *J. Mater. Chem.* **2012**, *22*, 21159−21166.

(8) Ge, L.; Han, C. C.; Liu, J. *Appl. Catal., B* **2011**, *108*, 100−107.

(9) Liao, G. Z.; Chen, S.; Quan, X.; Yu, H. T.; Zhao, H. M. *J. Mater. Chem.* **2012**, *22*, 2721−2726.

(10) Cheng, N. Y.; Tian, J. Q.; Liu, Q.; Ge, C. J.; Qusti, A. H.; Asiri, A. M.; Al-Youbi, A. O.; Sun, X. P. *ACS Appl. Mater. Interfaces* **2013**, *5*, 6815−6819.

(11) Tian, Y. L.; Chang, B. B.; Lu, J. L.; Fu, J.; Xi, F. N.; Dong, X. P. *ACS Appl. Mater. Interfaces* **2013**, *5*, 7079−7085.

(12) Niu, P.; Zhang, L. L.; Liu, G.; Cheng, H. M. *Adv. Funct. Mater.* **2012**, *22*, 4763−4770.

(13) Zhang, X. D.; Xie, X.; Wang, H.; Zhang, J. J.; Pan, B. C.; Xie, Y. *J. Am. Chem. Soc.* **2013**, *135*, 12−81.

(14) Yang, S. B.; Gong, Y. J.; Zhang, J. S.; Zhan, L.; Ma, L. L.; Fang, Z. Y.; Vajtai, R.; Wang, X. C.; Ajayan, P. M. *Adv. Mater.* **2013**, *25*, 2452−2456.

(15) Ye, S.; Qiu, L. G.; Yuan, Y. P.; Zhu, Y. J.; Xia, J.; Zhu, J. F. *J. Mater. Chem. A* **2013**, *1*, 3008−3015.

(16) Aranishi, K.; Jiang, H. L.; Akita, K.; Haruta, K.; Xu, Q. *Nano Res.* **2011**, *4*, 1233−1241.

(17) McDonald, K. J.; Choi, K. -S. *Chem. Mater.* **2011**, *23*, 4863−4869.

(18) Kong, L.; Jiang, Z.; Xiao, T. C.; Lu, L. F.; Jonesac, M. O.; Edwards, P. P. *Chem. Commun.* **2011**, *47*, 5512−5514.

(19) Hou, Y.; Li, X. Y.; Zhao, Q. D.; Quan, X.; Chen, G. H. *Environ. Sci. Technol.* **2010**, *44*, 5098−5013.

(20) Hou, Y.; Li, X. Y.; Zhao, Q. D.; Chen, G. H. *Appl. Catal., B* **2013**, *142*, 80−88.

(21) Wang, X. C.; Maeda, K.; Chen, X. F.; Takanabe, K.; Domen, K.; Hou, Y. D.; Fu, X. Z.; Antonietti, M. *J. Am. Chem. Soc.* **2009**, *131*, 1680−1681.

(22) Sui, J. H.; Zhang, C.; Hong, D.; Li, J.; Cheng, Q.; Li, Z. G.; Cai, W. *J. Mater. Chem.* **2012**, *22*, 13674−13681.

(23) Hong, J. D.; Xia, X. Y.; Wang, Y. S.; Xu, R. *J. Mater. Chem.* **2012**, *22*, 15006−15012.

(24) Teh, P. F.; Sharma, Y.; Pramana, S. S.; Srinivasan, M. *J. Mater. Chem.* **2011**, *21*, 14999−15008.

(25) Dong, G. H.; Zhao, K.; Zhang, L. Z. *Chem. Commun.* **2012**, *48*, 6178−6180.

(26) Subramanian, V.; Wolf, E. E.; Kamat, P. V. *J. Am. Chem. Soc.* **2004**, *126*, 4943−4950.

(27) Jassby, D.; Budarz, J. F.; Wiesner, M. *Environ. Sci. Technol.* **2012**, *46*, 6934−6941.

(28) Murdoch, M.; Waterhouse, G. I. N.; Nadeem, M. A.; Metson, J. B.; Keane, M. A.; Howe, R. F.; Llorca, J.; Idriss, H. *Nat. Chem.* **2011**, *3*, 489−492.

(29) Lu, J.; Do, I.; Drzal, L. T.; Worden, R. M.; Lee, I. *ACS Nano* **2008**, *2*, 1825−1832.

(30) Hou, Y.; Li, X. Y.; Zhao, Q. D.; Quan, X.; Chen, G. H. *Adv. Funct. Mater.* **2010**, *20*, 2165−2174.

(31) Chen, G. D.; Sun, M.; Wei, Q.; Zhang, Y. F.; Zhu, B. C.; Du, B. *J. Hazard. Mater.* **2013**, *244*, 86−93.

(32) Zhang, S. W.; Li, J. X.; Niu, H. H.; Xu, W. Q.; Xu, J. J.; Hu, W. P.; Wang, X. K. *ChemPlusChem* **2013**, *78*, 192−199.

(33) Tu, X. M.; Luo, S. L.; Chen, G. X.; Li, J. H. *Chem.—Eur. J.* **2012**, *18*, 14359−14366.

(34) Wang, Y. J.; Wang, Z. X.; Muhammad, S.; He, J. *CrystEngComm* **2012**, *14*, 5065−5070.

(35) Zhang, J. S.; Zhang, M. W.; Sun, R. Q.; Wang, X. C. *Angew. Chem., Int. Ed.* **2012**, *51*, 10145−10149.

(36) Wang, X. C.; Maeda, K.; Thomas, A.; Takanabe, K.; Xin, G.; Carlsson, J. M.; Domen, K.; Antonietti, M. *Nat. Mater.* **2009**, *8*, 76−80.

(37) Boumaza, S.; Boudjemaa, A.; Bouguelia, A.; Bouarab, R.; Trari, M. *Appl. Energy* **2010**, *87*, 2230−2236.

(38) Khodja, A. A.; Sehili, T.; Pilichowski, J. F.; Boule, P. *J. Photochem. Photobiol., A* **2001**, *14*, 231−239.

(39) Cui, Y. J.; Ding, Z. X.; Liu, P.; Antonietti, M.; Fu, X. Z.; Wang, X. C. *Phys. Chem. Chem. Phys.* **2012**, *14*, 1455−1462.

(40) Baciocchi, E.; Giacco, T. D.; Elisei, F.; Gerini, M. F.; Guerra, M.; Lapi, A.; Liberali, P. *J. Am. Chem. Soc.* **2003**, *125*, 16444−16454.

(41) Liu, G.; Niu, P.; Sun, C. H.; Smith, S. C.; Chen, Z. G.; Lu, G. Q.; Cheng, H. M. *J. Am. Chem. Soc.* **2010**, *132*, 11642−11648.

(42) Li, X. H.; Wang, X. C.; Antonietti, M. *Chem. Sci.* **2012**, *3*, 2170−2174.

(43) Dong, H. J; Chen, G.; Sun, J. X.; Li, C. M.; Yu, Y. G.; Chen, D. H. *Appl. Catal., B* **2013**, *134*, 46−54.

(44) Yan, T. J.; Long, J. L.; Shi, X. C.; Wang, D. H.; Li, Z. H.; Wang, X. X. *Environ. Sci. Technol.* **2010**, *44*, 1380−1385.